Silicon-Based Integrated Microwave Photonics

Weifeng Zhang, *Student Member, IEEE*, and Jianping Yao, *Fellow, IEEE*

(Invited Paper)

***Abstract*— Integrated microwave photonics is an emerging field in which photonic integrated technologies are employed to realize on-chip integration of microwave photonic systems with the aim to enrich the functionalities and enhance the system performance. Silicon photonics, as one of the various photonic integrated technology platforms, has attracted worldwide attention to achieve microwave photonic system integration for its compatibility with the current CMOS technology and its potential of seamless integration with electronics. In this paper, an overview about our recent work on silicon-based integrated microwave photonics is presented with an emphasis on silicon-based on-chip photonic arbitrary microwave waveform generation and microwave signals processing.**

***Index Terms*— Microwave photonics, silicon photonics, integrated photonics, photonic generation and processing of microwave signals.**

I. Introduction

MICROWAVE photonics is a field that studies the interactions between microwave and optical waves for the generation, processing, control and distribution of microwave signals by means of photonics [1]–[6]. The key motivation of using photonics for microwave applications is the wide bandwidth and low loss offered by modern photonics, which makes the implementation of certain important functions possible while in the electrical domain the same functions may not be realizable or the systems become extremely complicated and costly. In the past few years, there has been an increasing effort in researching microwave photonic techniques for different applications. Among the applications, photonic generation of arbitrary microwave waveforms [7] and photonic processing of microwave signals [8], [9] are two important topics and have been extensively studied.

Microwave waveforms with a large time-bandwidth product (TBWP) offer great potential for applications in communication systems to increase data transmission rate [10], [11] and in modern radar systems to enhance the range resolution [12]. Two types of microwave waveforms, frequency chirped and phase coded, are widely used. In the past, microwave waveforms were generated in the electrical domain using digital electronics [13], [14]. However, the time jitter, the limited speed and the nonlinearity of currently available digital-to-analog (DAC) converters set a limitation on the sampling rate, which inhibits from generating microwave waveforms at a high frequency with a large TBWP. To circumvent the obstacles, the generation of microwave waveforms in the optical domain has been considered a potential solution, which brings the inherent advantages of broad bandwidth and low loss offered by photonics to the microwave systems. In addition, the large flexibility in frequency tuning and system reconfiguration provides additional advantages. In the past few years, numerous approaches to the generation of frequency chirped and phase coded microwave waveforms based on photonics have been proposed and demonstrated [15]–[27].

Photonic processing of microwave signals has also been a topic of interest and has been intensively investigated in the last few years. Compared with the conventional microwave signal processing techniques based on digital or analog electronic circuits, photonic-assisted signal processing solutions provide a much higher speed, wider bandwidth and greater tuning range. Various techniques have been proposed and demonstrated. These signal processors include microwave filters [28], photonic temporal differentiators and integrators [29], Hilbert transformers [30], microwave mixers [31], and microwave phase shifters [32]. However, most of the signal processors were realized based on discrete components. For example, a photonic temporal differentiator, performing temporal differentiation of the complex envelope of an arbitrary optical signal, was demonstrated using a fiber Bragg grating (FBG) [29] for ultra-short pulse generation [33] and ultra-short pulse characterization [34]. Since the differentiator was implemented based on discrete components, the system was large and the stability was poor. For many applications, however, it is highly desirable that the signal processors are implemented using photonic integrated circuits (PICs).

A few demonstrations based on PICs have been recently reported [35], based on either silicon photonics [36]–[39] or III-V photonics [40]–[42]. For silicon-based PICs, the large refractive index contrast between silicon (n$\sim$3.47) and silica (n$\sim$1.45), and their optical transparency in the 1.55 μm wavelength window enable ultra-compact device dimensions, making it suitable for large-scale and high-density integration on a chip. In addition, the compatibility of silicon photonics with the current CMOS technology and its potential of seamless integration with electronics enable low-cost development of devices and systems with high volume production.

In this paper, we will discuss a few demonstrations based on silicon photonics for microwave waveform generation and microwave signal processing. Specifically, photonic generation of linearly chirped microwave waveforms (LCMWs) based

Manuscript received September 30, 2015; revised November 4, 2015; accepted November 9, 2015. Date of publication November 18, 2015; date of current version December 31, 2015. This work was supported by the Natural Sciences and Engineering Research Council of Canada.

The authors are with the Microwave Photonics Research Laboratory, School of Electrical Engineering and Computer Science, University of Ottawa, Ottawa, ON K1N6N5, Canada (e-mail: jpyao@eecs.uottawa.ca).

Color versions of one or more of the figures in this paper are available online at http://ieeexplore.ieee.org.

Digital Object Identifier 10.1109/JQE.2015.2501639

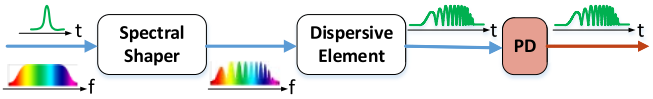

Fig. 1. Schematic of a microwave waveform generation system based on SS-WTT mapping technique.

on spectral shaping and wavelength-to-time (SS-WTT) mapping will be presented. Two silicon-based on-chip spectral shapers are designed, fabricated and characterized, and the use of the spectral shapers in an SS-WTT mapping system for LCMW generation will be discussed. Photonic processing of microwave signals will also be presented. A silicon-based phase-shifted waveguide Bragg grating (PS-WBG) as a single channel temporal differentiator and a silicon-based multiple cascaded microring resonators (MRRs) as a multiple channel temporal differentiator are designed, fabricated and demonstrated. In addition, a silicon-based electrically tunable sidewall-Bragg-grating Fabry-Perot filter (SBG-FPF) as a reconfigurable signal processor to achieve different signal processing functions is also presented.

The paper is organized as follows. In Section II, photonic generation of microwave waveforms based on SS-WTT mapping is described, followed by two demonstrations using silicon-based spectral shapers to perform spectral shaping for LCMW generation. In Section III, photonic temporal differentiation is described, followed by two demonstrations to implement a single channel and multiple channel temporal differentiation with independently tunable differentiation orders. In addition, a silicon-based electrically tunable SBG-FPF reconfigurable for multi-function signal processing is discussed. In Section IV, a conclusion is drawn.

II. Photonic Generation of Microwave Waveforms

Among the different types of microwave waveforms, LCMWs are widely used for radar and communications systems and have been widely studied. In general, an LCMW can be generated by beating two complementarily parabolically phase-modulated optical pulses [17], [18] or simply two linearly chirped optical pulses with different chirp rates [19]–[21]. An LCMW can also be generated based on direct space-to-time (DST) mapping [22], [23], and SS-WTT mapping [24]–[27].

If two optical wavelengths are complementarily phase modulated by a parabolic microwave waveform [17], [18] or two linearly chirped optical pulses with different chirp rates [19]–[21] are applied to a photodetector (PD), an LCMW is generated.

In a DST mapping system, an ultrashort optical pulse is launched into an optical pulse shaper to generate a pulse burst with increasing or decreasing temporal spacing. After detection at a PD, an LCMW with its chirp rate determined by the profile of the temporal spacing is generated [22], [23].

An LCWM can also be generated based on SS-WTT mapping. Fig. 1 shows a typical SS-WTT mapping system, which consists of an ultrashort optical pulse source, an optical spectral shaper, a dispersive element, and a high-speed PD. An ultrashort optical pulse is spectrally shaped by the optical

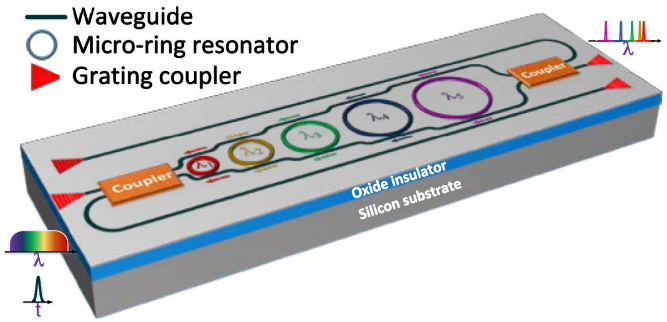

Fig. 2. Perspective view of a silicon-based on-chip spectral shaper consisting of five MRRs.

spectral shaper. The spectrum-shaped optical pulse is then sent to the dispersive element to perform linear WTT mapping. At the output of the high-speed PD, a microwave waveform with the shape identical to that of the shaped optical spectrum is generated. For LCMW generation, the optical spectral shaper should have a spectral response with an increasing or decreasing free spectral range (FSR). The approach based on SS-WTT mapping provides large flexibility, since the spectral response of the spectral shaper can be easily reconfigured. For example, in [27], a spectral shaper having a Mach-Zehnder interferometer (MZI) structure incorporating an optically pumped linearly chirped fiber Bragg grating (LC-FBG) written in an erbium-ytterbium co-doped fiber in one arm was demonstrated for chirp-rate tunable LCMW generation. By optically pumping the LC-FBG with a different pumping power, the chirp rate of the generated LCMW was tuned. In the demonstration, an LCMW with a tunable chirp rate from 79 to 64 GHz/ns was generated.

The key component in an SS-WTT mapping system is the spectral shaper. The spectral shapers in most of the approaches reported in the past were implemented based on either free-space optics [24] or fiber optics [25]–[27]. Thus the size is large and the stability is poor. To have a spectral shaper with a small size and a good stability, integrated solutions should be adopted. For example, in [38] an on-chip spectral shaper implemented based on silicon photonics was demonstrated. The spectral shaper was designed to have multiple cascaded MRRs. By thermally tuning the MRRs, a spectral shaper with an increasing or decreasing FSR is obtained. The generation of an LCMW with a chirp rate of 8 GHz/ns was demonstrated. Thermal tuning enables the reconfigurability of the system for arbitrary microwave waveform generation. However, due to the limited tuning range, the chirp rate of the generated LCMWs is limited.

To generate an LCMW with a large chirp rate, recently we have designed and demonstrated two optical spectral shapers based on silicon photonics, both are fabricated using a CMOS-compatible technology with 193-nm deep ultraviolet lithography.

The first spectral shaper consists of multiple cascaded MRRs with largely different radii, as shown in Fig. 2. The small footprint of an MRR makes it highly suitable for high-density integration, and thus is being extensively

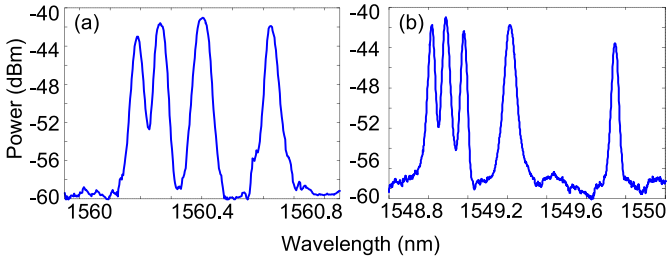

Fig. 3. Measured spectral response of an on-chip spectral shaper consisting of (a) four cascaded MRRs and (b) five cascaded MRRs.

researched recently [43]. The spectral shaper has an MZI structure incorporating multiple cascaded MRRs [44]. As can be seen, an incident light beam is split by the first adiabatic 3-dB coupler [45] into two beams that travel through the upper and lower arms of the MZI. Each ring will selectively transfer the optical power at its resonance wavelength from the through-port waveguide to its drop-port waveguide. The different colors of the rings shown in Fig. 2 indicate that each ring is designed to have a different radius and therefore a different resonant wavelength. The spacing between two neighboring rings is large enough to avoid mutual interferences. In the upper and lower waveguides, S-shape waveguide bends, which are designed using Bezier curves to minimize the mode mismatch and thus reduce the waveguide bending loss [46], are added to accommodate to the change of the rings. The resonant wavelengths from the both waveguides will be recombined at the first adiabatic 3-dB coupler and constructively interfere as reflected signals. The non-resonant wavelengths are recombined at the second adiabatic 3-dB coupler at the transmission port. In order to achieve a maximum reflection power, each ring is designed to work in the critical coupling condition. By carefully designing the ring radii, at the reflection port, the reflection peaks with a linearly increasing spacing can be achieved.

Fig. 3(a) shows the spectral response at the reflection port of an on-chip spectral shaper consisting of four MRRs and Fig. 3(b) shows the spectral response of an on-chip spectral shaper consisting of five MRRs. As can be seen, the spacing between the neighboring peaks is linearly increasing, which is required for LCMW generation. Fig. 4(a) shows the experimentally generated LCMW using the four-ring spectral shaper in the SS-WTT mapping system, and Fig. 4(b) shows the spectrogram of the generated LCMW, which illustrates the time distribution of the microwave frequency components. The colors indicate the relative spectral intensity of the frequency components. Low-frequency contents below 5 GHz are not shown in the spectrogram. As can be seen the generated LCMW has a bandwidth of 8.5 GHz and a chirp rate of 12.2 GHz/ns. Fig. 4(c) shows the experimentally generated LCMW using the five-ring pulse shaper, and the spectrogram is shown in Fig. 4(d). As can be seen, the generated LCMW has a bandwidth of 15.5 GHz and a chirp rate of 17.2 GHz/ns. Small differences between the spectral response of the spectral shaper and its corresponding generated LCMW are observed, which are mainly due to the limited bandwidth of the PD. Due to the limited bandwidth of the PD, the high frequency components are attenuated.

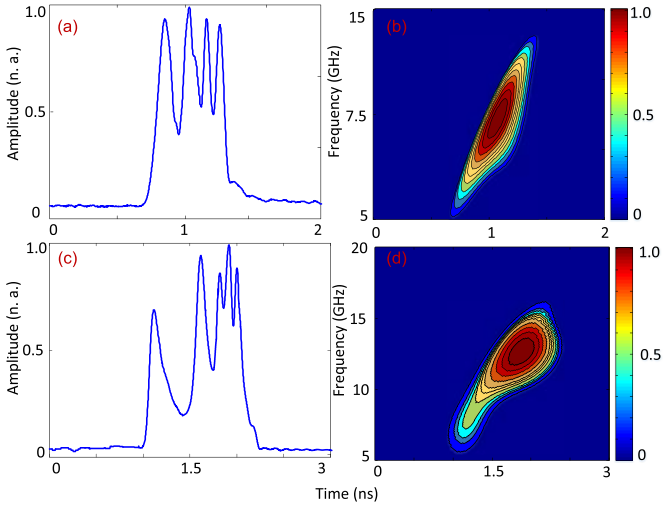

Fig. 4. (a) Generated LCMW and (b) its spectrogram when using an on-chip spectral shaper consisting of four cascaded MRRs. (c) Generated LCMW and (d) its spectrogram when using on-chip spectral shaper consisting of five cascaded MRRs.

Compared with the work in [38], the distinct feature of this optical spectral shaper is that the MRRs are designed to have largely different radii for the generation of an LCMW with a much higher chirp rate. Thanks to the S-shape waveguide bends in the MZI arms, the MRRs can be accommodated into the two arms smoothly, which gives the advantages in incorporating more different rings and increasing the compactness of the device. In addition, the spectral shaper works in the reflection mode, thus the reflection port and the input port can share a common grating coupler, which could further reduce the footprint. However, due to a limited number of MRRs, the generated LCMW has a TBWP as small as 18.7. For practical applications where large pulse compression is required, an LCMW with a much greater TBWP is needed.

The second spectral shaper is designed to have a greater TBWP [47], [48]. Fig. 5 illustrates the perspective view of the second spectral shaper. The inset shows the structures of the strip waveguide and rib waveguide used in the chip. Fig. 6(a) presents the schematic layout of the spectral shaper, which has an MZI structure that incorporates two identical LC-WBGs with opposite chirp rates in its two arms. An input light wave is split by a compact Y-branch [49] into two beams to travel through the LC-WBGs in the upper and lower arms. Spectral components of the light waves of different wavelengths are reflected from different positions in the LC-WBGs. By the second and the third Y-branches, the reflected light waves are collected and recombined at the fourth Y-branch. The combined light wave is guided to an output grating coupler to couple the light out of the chip. When recombined, due to the optical interference, the optical spectral shaper has a spectral response with a wavelength-dependent FSR, which is required to generate an LCMW. The central frequency of the generated LCMW can be controlled by using an offset waveguide added in the lower arm of the spectral shaper to control the length difference between the two arms. By designing the LC-WBGs and choosing the length of the offset waveguide, the spectral response of the spectral

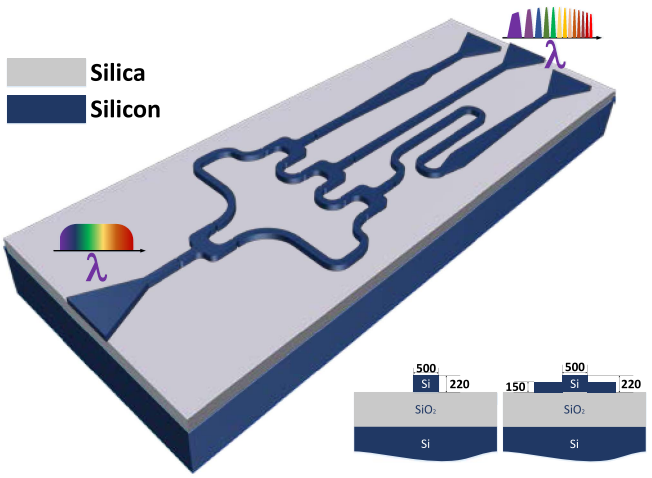

Fig. 5. Perspective view of the silicon-based on-chip optical spectral shaper incorporating LC-WBGs. (Inset: (Left) Wire waveguide and (Right) Rib waveguide).

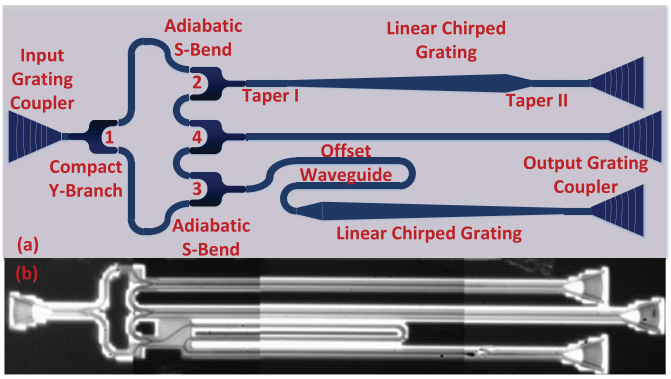

Fig. 6. (a) Schematic layout of the designed on-chip spectral shaper; (b) Image of the fabricated spectral shaper with the length of the offset waveguide equal to the length of the LC-WBG captured by a microscope camera.

shaper can be controlled to have a symmetrical, a uniformly increasing or decreasing FSR, which is required for LCMW generation. Fig. 6(b) shows the image of a fabricated spectral shaper captured by a microscope camera.

The two LC-WBGs are the key components in the spectral shaper. Fig. 7 shows the perspective view of a designed LC-WBG. Different from the work in [50], the grating is realized by introducing periodic sidewall corrugations on the slab. By keeping the grating period uniform and linearly increasing the width of the rib along the grating, a linear chirp is produced since the effective refractive index is linearly increasing as the rib width increases in a definite range. The inset in Fig. 7 shows the simulated fundamental TE mode profile in the rib waveguide with a rib width of 500 nm (left) and 650 nm (right).

Fig. 8(a), (b) and (c) show the measured reflection spectrum in blue and the group delay in green of the fabricated LC-WBG with the rib width linearly increasing from 500 to 550 nm, 500 to 600 nm, and 500 to 650 nm, respectively. As can be seen, by controlling the rib width, it is convenient to tailor the reflection response and the chirp rate

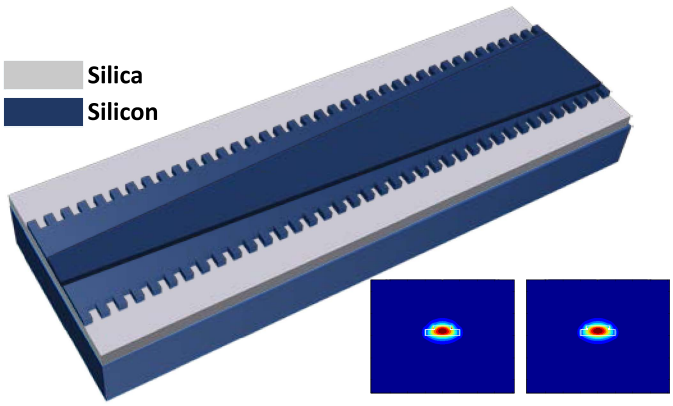

Fig. 7. Perspective view of an LC-WBG. (Inset: Simulated fundamental TE mode profile of the rib waveguide with the rib width of 500 nm (left) and 650 nm (right)).

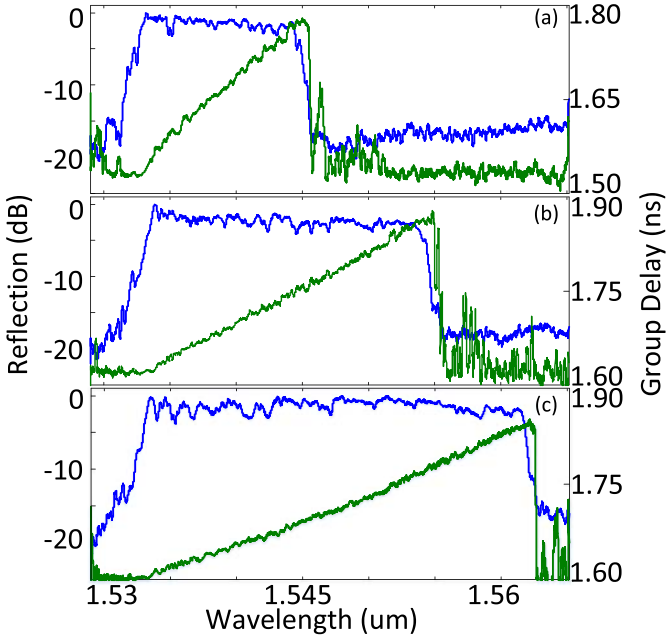

Fig. 8. Measured spectral and group delay responses of an LC-WBG with the rib width linearly increasing from 500 to (a) 550 nm, (b) 600 nm, and (c) 650 nm.

TABLE I
PROPERTIES OF LC-WBGs*

Rib Width (nm)	Bandwidth (nm)	Delay (ps)	Dispersion (ps/nm)	Chirp Rate (nm/mm)
550	1533~1544	228	20.7	0.88
600	1534~1554	236	11.8	1.59
650	1533~1562	241	8.3	2.31

* Each LC-WBG has a linearly increasing rib width starting from 500 nm.

of an LC-WBG. Table I presents the reflection bandwidth, time delay, dispersion and chirp rate of each of the LC-WBGs in Fig. 8. The easiness in tailoring the spectrum and the chirp rate enables the LC-WBG to have large flexibility in satisfying the specific demands such as dispersion engineering. It is worth noting that all the reflection spectrums in Fig. 8 are normalized. The insertion loss for the three LC-WBGs is around 23 dB, most of which is induced by the coupling loss

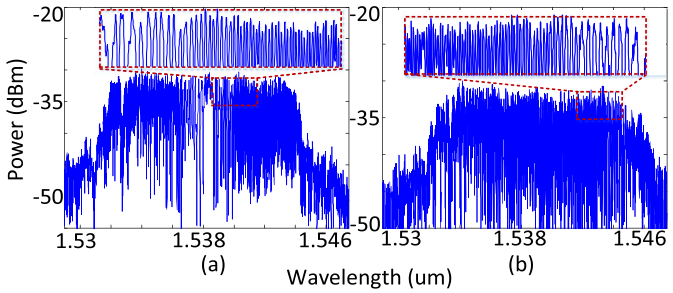

Fig. 9. Measured spectral response of a fabricated spectral shaper when the length of the offset waveguide is equal to (a) zero, and (b) the length of the LC-WBG.

of the grating coupler and the splitting loss of the compact Y-branch. By optimizing the design of the grating coupler, the insertion loss of the LC-WBG could be largely reduced.

The advantage of achieving the chirp by varying the rib width is that the grating period is uniform, which is more robust than varying the grating period [51]. The reflection spectrum and the chirp rate can be tailored in a simple way of controlling the rib width. In addition, the LC-WBG is able to work as an optical delay line, which is a key device in the applications such as data buffering in optical switches [52] and optical beamforming in phased-array antennas [53]. Furthermore, compared with other integrated delay lines comprising of MRRs or photonic crystal waveguides [54], such an LC-WBG provides a broader bandwidth and a comparatively smaller optical transmission loss. More importantly, such an LC-WBG is capable of functioning as a dispersive element in an SS-WTT mapping system. Thus, it is feasible to integrate an optical spectral shaper and a dispersive element on a single chip, which is a significant step further to implement a fully integrated SS-WTT mapping system.

By incorporating a pair of LC-WBGs with the rib width linearly increasing from 500 to 550 nm, a spectral shaper is implemented. Fig. 9(a) shows the measured spectral response of a fabricated spectral shaper with the length of the offset waveguide equal to zero, and the inset shows the zoom-in view of a small segment of the spectral response. As can be seen, the spectral response presents a symmetrical FSR, and the FSR is linearly increasing on both sides. Fig. 9(b) shows the measured spectral response of a fabricated spectral shaper with the length of the offset waveguide equal to the length of the LC-WBG and the inset shows the zoom-in view of a small segment of the spectral response. The spectral response presents a linearly decreasing FSR. Both of the fabricated spectral shapers exhibit a linearly varying FSR, which fully meet the requirements of a spectral shaper imposed by the SS-WTT mapping technique.

By incorporating the on-chip spectral shaper with the length of the offset waveguide equal to zero into an SS-WTT mapping system, an LCMW with a symmetrical chirp profile is generated. Fig. 10(a) shows an LCMW which has a symmetrical chirp profile. The pulse duration is around 10.90 ns. Fig. 10(b) shows the spectrogram of the generated LCMW, in which the waveform is linearly chirped with a symmetrical chirp profile. To further evaluate the chirp of the waveform, the instantaneous microwave frequency is also calculated based on the Hilbert transform [55] and presented by the red-dotted line in Fig. 10(b), which agrees well with the spectrogram. The central frequency of the generated symmetrically chirped microwave waveform is 1.2 GHz, which is different from the theoretical prediction of 0 GHz. This difference is resulted from a slight asymmetry between the two arms of the MZI structure in the spectral shaper induced by fabrication imperfections. On the right side of the center, the instantaneous frequency is linearly increasing with a positive chirp rate of 5.4 GHz/ns, while on the left side of the center, the instantaneous frequency is linearly decreasing with a negative chirp rate of −4.9 GHz/ns. This small difference in the chirp rates is resulted from the small asymmetry between the two LC-WBGs in the two arms of the MZI, induced by fabrication imperfections again. According to the time-domain waveform and its carrier frequency distribution, the TBWP of the generated LCMW is estimated to be around 359.7. Fig. 10(c) shows the compressed pulse with a pulse width of 24 ps, which is obtained by calculating the autocorrelation of the generated microwave waveform. By comparing the pulse width of the waveforms in Fig. 10(a) and (c), a pulse compression ratio as large as 454.2 is obtained.

By incorporating the on-chip spectral shaper with the length of the offset waveguide equal to the length of the LC-WBG into the SS-WTT mapping system, an LCMW with a monotonically and linearly increasing chirp is generated. Fig. 10(d) shows an experimentally generated LCMW with a linearly increasing chirp. The pulse duration is around 20.5 ns. Fig. 10(e) shows the spectrogram plot of the generated LCMW and the instantaneous microwave frequency in the red-dotted line. Again, the results match well. The center frequency of the generated LCMW is 15.8 GHz, which agrees well with the theoretical prediction of 16.4 GHz. The LCMW has a positive chirp rate of 1.54 GHz/ns. According to the time-domain waveform and its carrier frequency distribution, the TBWP of the generated LCMW is estimated to be around 615. Fig. 10(f) shows the compressed pulse with a pulse width of 32.9 ps. By comparing the pulse width of the waveforms in Fig. 10(d) and (f), a pulse compression ratio as large as 623.1 is obtained.

The key feature of the spectral shaper is that an LCMW with a large chirp rate and a large TBWP can be generated, which is achieved by incorporating a pair of LC-WBGs with large and opposite chirp rates in the spectral shaper. In addition, it is interesting to observe from the experimental results in Fig. 10 that as the length of the offset waveguide in the spectral shaper is varied from zero to the length of the LC-WBG, the central frequency of the generated LCMWs is changed from 1.2 to 15.8 GHz. The offset waveguide with different lengths leads to a different central frequency of the generated LCMW, which will bring benefit to the generation of an LCMW with a tunable central frequency, chirp rate and TBWP.

We also evaluate the generation of an LCMW with a tunable central frequency by changing the center wavelength of the input ultra-short pulse. In the experiment, a spectral shaper incorporating a pair of LC-WBGs with the rib waveguide width linearly increasing from 500 to 600 nm is incorporated into the SS-WTT mapping system. Fig. 11 shows the measured spectral response of the spectral shaper with the length of the

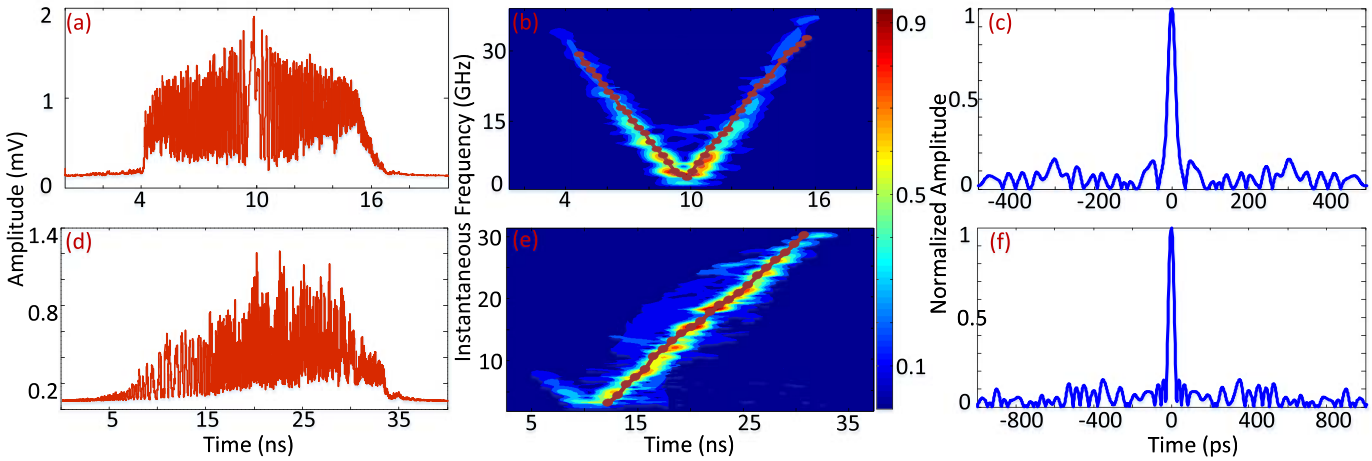

Fig. 10. Experimental results of on-chip spectral shaper with the length of the offset waveguide equal to zero: (a) the generated LCMW, (b) the spectrogram and instantaneous frequency of the generated LCMW, and (c) the compressed pulse; Experimental results of on-chip spectral shaper with the length of the offset waveguide equal to the length of the LC-WBG: (d) the generated LCMW, (e) the spectrogram and instantaneous frequency, and (f) the compressed pulse.

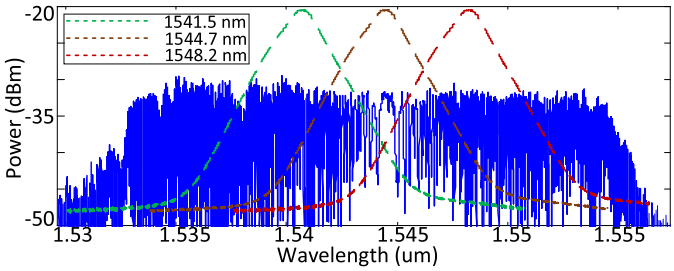

Fig. 11. Measured spectral response of a fabricated spectral shaper with the rib waveguide width in the LC-WBGs linearly increasing from 500 to 600 nm when the length of the offset waveguide is equal to zero. (The dashed line is the input optical pulse spectrum with the different center wavelength from a tunable MLL.).

offset waveguide equal to zero, and the dashed line presents the input optical pulse spectrum with the different center wavelength from a tunable MLL. As can be seen, the spectral response presents a symmetrical FSR, and the FSR is linearly increasing on both sides. Due to the strong index modulation in the waveguide gratings [56], the reflection bandwidths of the LC-WBGs are very broad, which leads to a broader working bandwidth of the spectral shaper than the input optical pulse spectra width. Thus, by locating the center wavelength of the input pulse at different positions along the gratings, the path difference between the two arms of the MZI is different, which is equivalent to varying the length of the offset waveguide. Therefore, by tuning the central wavelength of the input optical pulse, the central frequency of the generated LCMW is tuned.

Fig. 12 illustrates the experimentally generated LCMWs when the center wavelength of the input optical pulse is tuned at 1541.5 nm, 1544.7 nm, and 1548.2 nm. It is clear to see that as the center wavelength of the input optical pulse is changed, the central frequency of the generated LCMWs is changed. In addition, the chirp profile of the generated LCMW is varied from a linearly increasing chirp profile, to a symmetrical chirp profile, to a linearly decreasing chirp profile.

TABLE II
PROPERTIES OF THE GENERATED LCMWS

Generated LCMWs	Chirp Rate (GHz/ns)*	TBWP	Compression Ratio
Fig. 11(a)	+4.9	238	250
Fig.11(d)	-4.4, +4.8	107	132
Fig. 11(g)	-4.9	229	260

*The plus sign represents a linearly increasing chirp profile, while the minus sign represents a linearly decreasing chirp profile.

Table II lists the chirp rates, TBWPs and compression ratios of the generated LCMWs.

Thanks to the strong index modulation in the waveguide gratings, the broad bandwidth of the LC-WBGs enables the spectral shaper to have a broader spectral width than the input optical pulse. Thus, by varying the center wavelength of the input optical pulse, the central frequency of the generated LCMW could be tuned. In addition, by taking advantage of plasma dispersion effect in silicon [57], it is appealing to realize an electrically tunable LC-WBG and thus an electrically tunable spectral shaper. Then, it is feasible to integrate an electrically tunable optical spectral shaper and an electrically tunable dispersive element on a single chip, which offers full reconfigurability of the system in terms of central frequency and chirp rate tuning of the generated LCMW.

III. PHOTONIC PROCESSING OF MICROWAVE SIGNALS

Processing microwave signals in the optical domain by taking advantage of the low loss and large bandwidth offered by modern photonics has been a topic of interest in recent years, and numerous processing solutions have been proposed and demonstrated, including microwave filtering, differentiation, integration, Hilbert transformation, and microwave mixing. As one of the basic signal processing blocks, a photonic temporal differentiator is used to perform temporal differentiation of the complex envelope of an arbitrary optical signal. In general, a photonic temporal differentiator can be realized using an optical device that has a transfer function

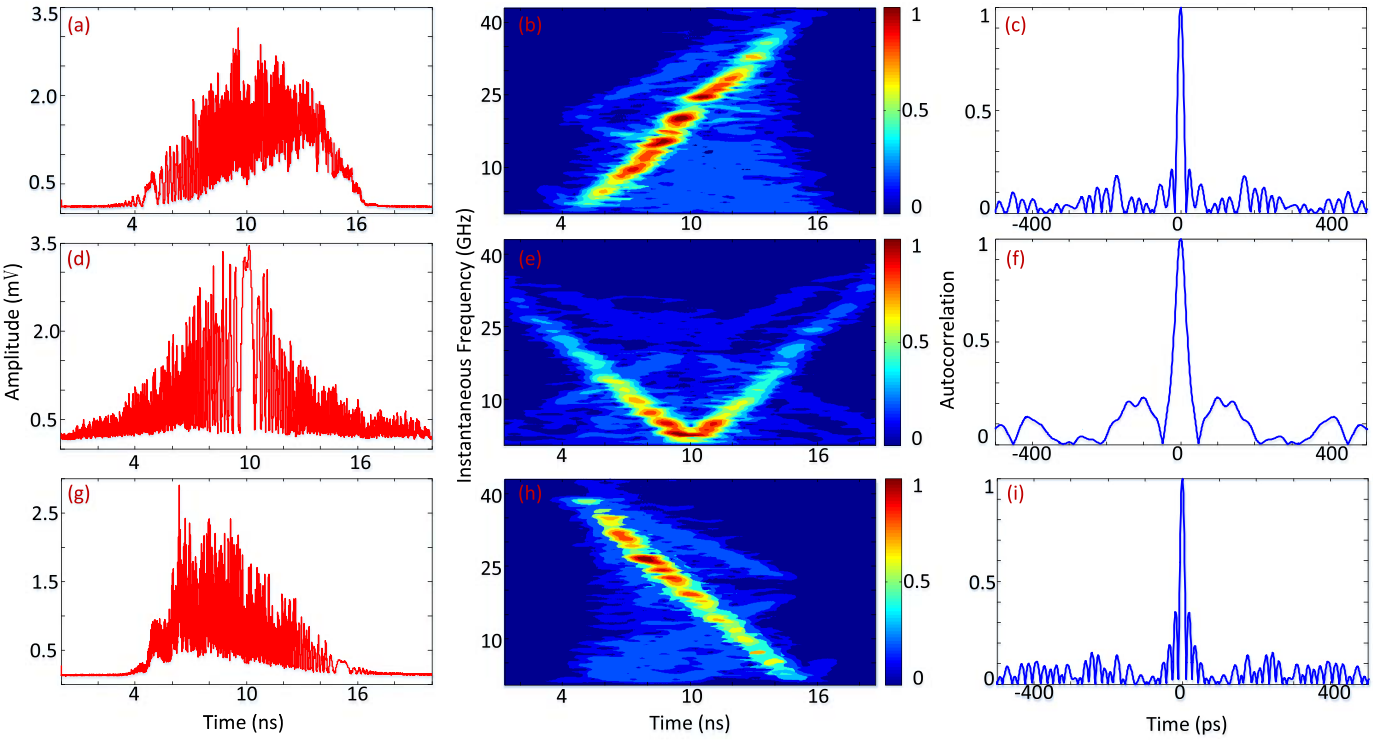

Fig. 12. Experimental results using an on-chip spectral shaper with the length of the offset waveguide equal to zero when the center wavelength of the input optical pulse is 1541.5 nm, 1544.7 nm, and 1548.2 nm, respectively: (a) the generated LCMW, (b) the spectrogram, and (c) the compressed pulse; (d) the generated LCMW, (e) the spectrogram, and (f) the compressed; (g) the generated LCMW, (h) the spectrogram, and (i) the compressed pulse.

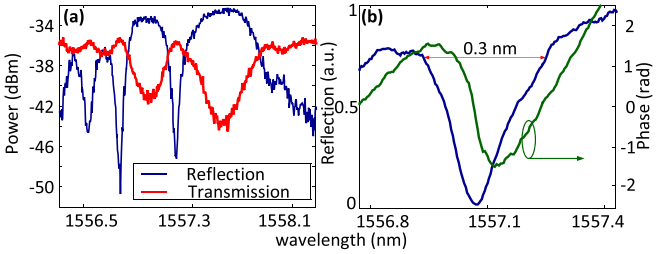

Fig. 13. (a) Measured reflection and transmission spectral responses of the fabricated PS-WBG on a ridge waveguide with a designed corrugation width of 125 nm. (b) Zoom-in view of the reflection notch and its phase response.

given by $[j(\omega-\omega_0)]^n$, where n is the differentiation order, ω is the optical frequency and ω_0 is the optical carrier frequency. When the differentiation order n is not one, the processor is generalized to be a fractional-order photonic temporal differentiator [58], [59]. Different schemes to implement a photonic temporal differentiator have been proposed, mainly based on fiber-optics [60], [61]. Again, to reduce the size and enhance the stability, integrated solutions are highly needed. Recently we have designed and demonstrated two temporal differentiators based on silicon photonics, with one for single channel operation [62] and the other for multiple channel operation [63]. The two temporal differentiators are fabricated using a CMOS-compatible technology with 248-nm and 193-nm deep ultraviolet lithography, respectively.

First, a photonic temporal differentiator implemented using a PS-WBG in a single-mode ridge waveguide is discussed [62]. The silicon-based PS-WBG is designed to have a wide reflection notch by creating deep corrugations on the sidewalls of the ridge. Fig. 13(a) shows the reflection and transmission spectra of the PS-WBG. It can be seen there is a resonant transmission window within the stop band in the transmission spectrum. In order to implement the optical differentiator, the gratings are deliberately designed to have a wide reflection notch by increasing the depth of the corrugations. Fig. 13(b) shows the width of the reflection notch (top-to-top width) of the fabricated PS-WBG is approximately 0.3 nm (or 37.5 GHz), and the phase response shows there is a phase jump of π at the Bragg wavelength.

Fig. 14(a) shows the input Gaussian pulse (blue-solid line) and a simulated Gaussian pulse (red-dashed line) for comparison. The ripples observed at the tails of the measured Gaussian pulse are resulted from the limited sampling rate of a real-time oscilloscope. Fig. 14(b) shows the corresponding temporally differentiated pulse (blue-solid line) generated using the PS-WBG and the simulated temporally differentiated pulse (red-dashed line). As can be seen the experimentally generated pulse is close to the simulated pulse, which confirms effectiveness of the use of the PS-WBG to perform a first-order differentiation. Same ripples are observed in the experimentally generated pulse, and the dip in the center of the experimentally differentiated pulse is not as deep as the simulated pulse, which is mainly caused by the limited bandwidth of the PD.

The key advantage when using a silicon-based PS-WBG to realize a photonic temporal differentiation is that the PS-WBG has a compact size and a higher fabrication tolerance. However, an untunable differentiation order places an obstacle

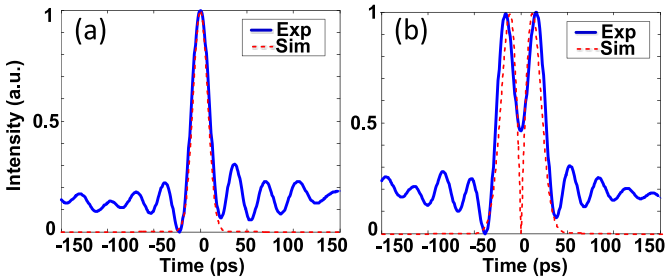

Fig. 14. (a) An input Gaussian pulse with an FWHM of 25 ps, and (b) the temporally differentiated pulses by simulation and experiment.

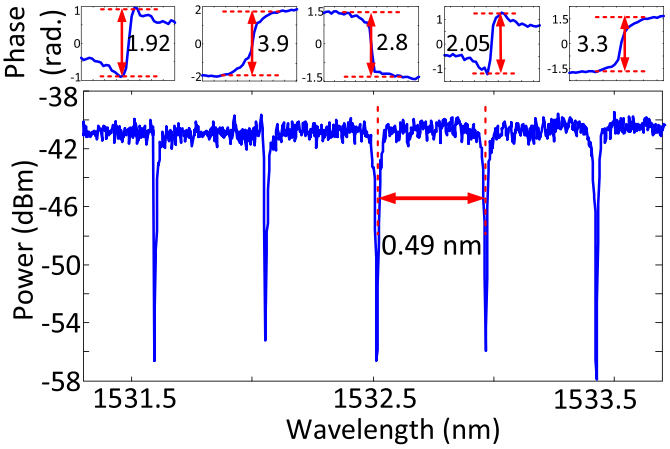

Fig. 15. Measured spectral response of the five-channel fractional-order temporal differentiator; Inset: measured phase response of the five-channel fractional-order temporal differentiator.

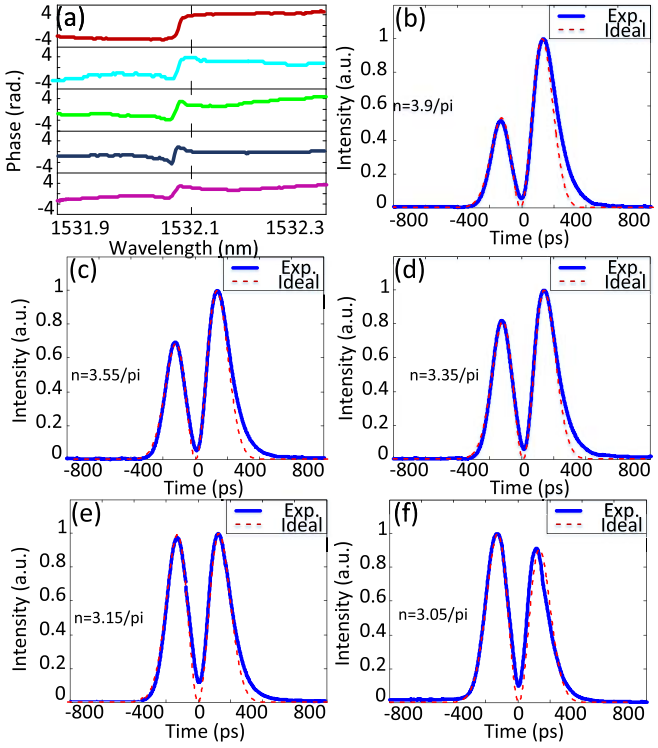

Fig. 16. Experimental results for differentiation order tuning. (a) Measured phase response of the second channel with the power of the pump light increased, and measured differentiated output pulses from the photonic fractional differentiator at the second channel with the pump light wave power of (b) 0 dBm, (c) 21.7 dBm, (d) 25 dBm, (e) 28.7 dBm, and (f) 31 dBm.

for widespread applications. In addition, with the fast growth of information exchange all over the world, wavelength-division multiplexing (WDM), as a promising technology for expanding the capacity for optical communications, has been widely used in the present optical communications networks [64]. For ultrafast signal processing and characterization in a WDM network, a photonic temporal differentiator that is capable of performing temporal differentiation of multiple channel signals carried by multiple wavelengths is required. In the silicon-based PS-WBG temporal differentiator, the channel number is always one.

To overcome the issues such as the tunability of differentiation order and the channel number, a multiple channel fractional-order temporal differentiator with independently tunable differentiation orders was proposed [63]. The structure of the multiple channel differentiator is the same as that shown in Fig. 2 except the radii of the MRRs are particularly selected to make the channels fit the WDM grid and the device works in the transmission mode. By controlling the radii of the MRRs, a multiple channel spectral response with uniform channel spacing is achieved, which is used to function as a multiple channel temporal differentiator with multiple sub-differentiators.

Fig. 15 shows the spectral response of a five-channel fractional-order temporal differentiator with a channel spacing of 0.49 nm. The inset presents the phase response for each of the five channels. Taking the third channel as an example, the channel has a bandwidth of 0.032 nm or 4 GHz, which can be used for the implementation of a photonic differentiator with an operation bandwidth of 4 GHz. Furthermore, the differentiation order of each sub-differentiator is independently tunable by optically pumping the corresponding MRR, which leads to the phase change in the spectral response due to the two-photon absorption (TPA) induced nonlinear effect [65]. Based on the 3-dB bandwidth of the third channel, the Q-factor of the MRR is calculated to be 4×10^5. A high Q-factor ensures an MRR to have a strong capacity in light confinement, which enables relatively low power pumping of the MRR to introduce the required phase response change. Meanwhile, a high Q-factor makes an MRR to have a relatively small bandwidth. Thus, a trade-off is imposed between the operation bandwidth and the required pumping power.

When a pumping light wave is fed into the specific MRR, the TPA-induced nonlinear effect could lead to a change in the phase response of the MRR. By varying the power level of the pumping light, the phase response is changed. Thus, the differentiation order of this MRR as a temporal differentiator is tuned. Fig. 16 shows the experimental result of the differentiation order tuning on the second channel. A single probe Gaussian pulse, of which the central wavelength is aligned to the center of second channel, is applied to the chip. With an optical coupler, a pump light wave is launched into the chip, too. The wavelength of the pumping light is different from the wavelength of the probe light, but is located at one resonant wavelength of the MRR to increase the light confinement. Fig. 16(a) shows the measured phase response of the second channel with the pumping power increased from 0 to 31 dBm. As can be seen, with the increase of the pump

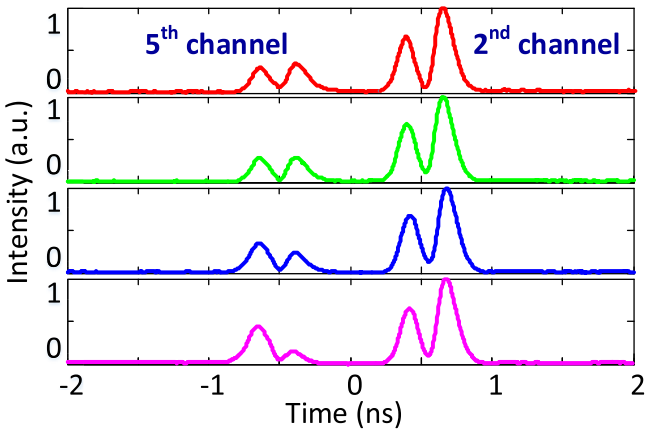

Fig. 17. Experimental results for independent tunability of the differentiation order.

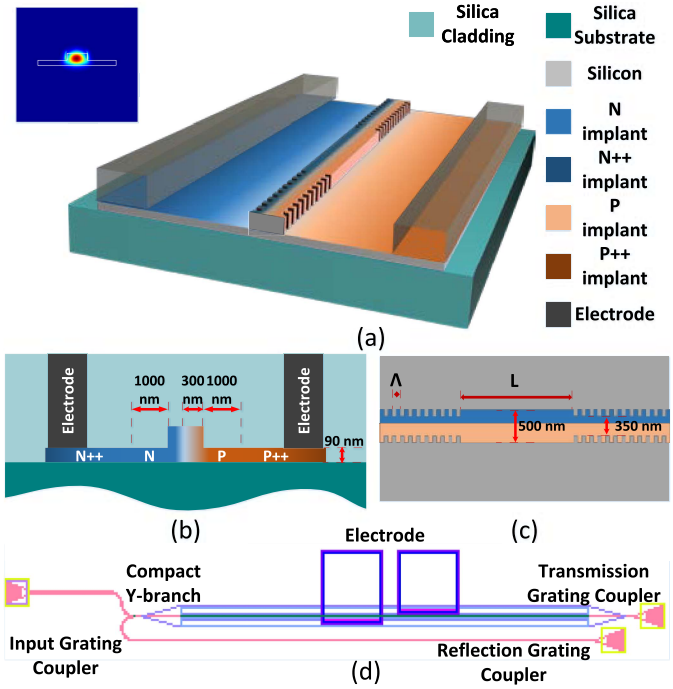

Fig. 18. (a) Perspective view of the proposed SBG-FPF. (Inset: Simulated fundamental TE mode profile of the rib waveguide) (b) Cross-sectional view of proposed SBG-FPF. (c) Top view of the FP cavity. (d) Schematic layout of the proposed SBG-FPF.

light power, the phase jump becomes smaller, which is resulted from the increase in the internal loss in the MRR due to the TPA-induced nonlinear effect. Fig. 16(b)-16(f) show the corresponding temporally differentiated pulses (blue-solid line). Differentiated pulses with differentiation orders of 1.24, 1.13, 1.07, 1.00, and 0.97 are generated. The simulated pulses with an ideal input Gaussian pulse and an ideal differentiator with the same orders are also shown (red-dashed line) for comparison, which confirms the effectiveness of the use of the device to perform a tunable fractional-order differentiator.

Since the spacing between the neighboring MRRs are far enough to avoid the mutual interference, the differentiation order of each ring can be independently tuned without the influence on the neighboring MRRs. Fig. 17 shows the experimental result of independent tuning of the differentiation order on the fifth channel, while the differentiation order of the second channel is not affected. Two probe light waves are sent to the chip at two resonant wavelengths of the second and the fifth channels. The measured differentiated pulses at the output of the differentiator are shown in Fig. 17. The pulses on the left correspond to the output from the fifth channel and on the right correspond to the output from the second channel. The magnitude difference between the differentiated pulses from the two channels is resulted from the different amplitude resonances of the two channels. When the pumping wavelength is selected corresponding to another resonant wavelength of the fifth channel and the power is increased from 0 to 31 dBm, the order of the differentiated pulse at the output fifth channel is changed while the order of the differentiated pulse at the second channel maintains unchanged, which confirms that the differentiation order of each sub-differentiator in this integrated on-chip multiple channel differentiator is independently tuned.

The key feature of this multiple channel temporal differentiator is that a WDM signal at multiple wavelengths can be simultaneously differentiated and the fractional order

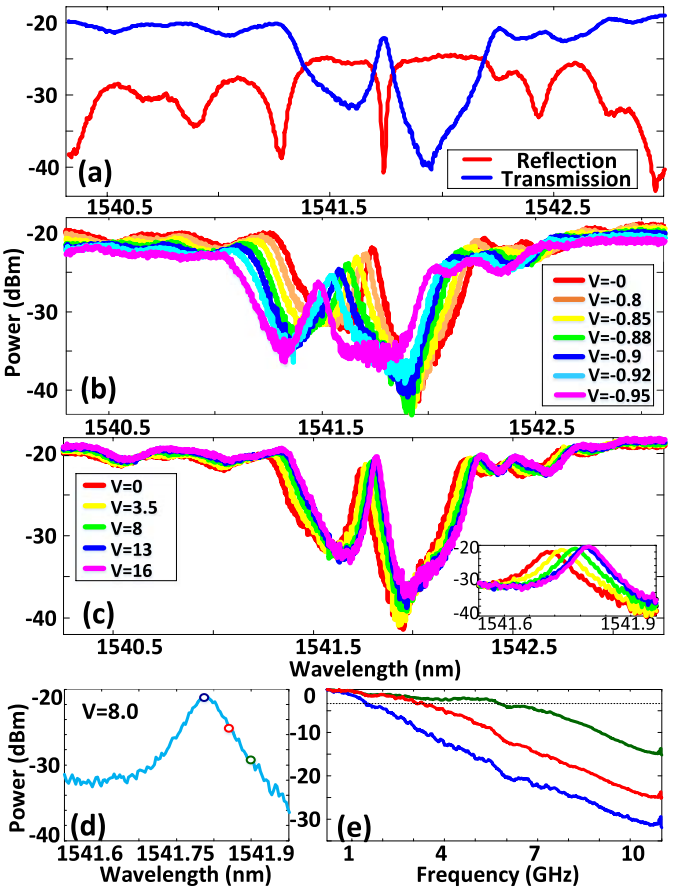

Fig. 19. (a) Measured reflection and transmission spectra of the SBG-FPF with a zero bias voltage applied. (b) Wavelength shift of the transmission spectrum when forward biased. (c) Wavelength shift of the transmission spectrum when reverse biased (Inset: Zoom-in view of the wavelength shift of the transmission window). (d) Measured transmission window of the SBG-FPF when reverse biased with a voltage of 8.0 V. (e) Measured frequency responses for three different wavelengths when the reverse bias voltage is 8.0 V.

of each individual channel can be independently tuned, which gives more flexibility in WDM signal processing.

However, the tunability of the differentiation order is achieved via TPA-induced thermal optics. The response time as slow as micro-seconds would limit the tuning speed. To boost the tuning speed, plasma dispersion effect in silicon is a strong candidate for the realization of tunability. In [66], we demonstrated a silicon-based on-chip electrically tunable SBG-FPF. Fig. 18(a) illustrates the perspective view of the SBG-FPF, in which the cladding layer of silica is removed in order to clearly illustrate the internal structure of the device. The inset in Fig. 18(a) shows a simulated mode profile of the fundamental TE mode at 1550 nm. To increase the tuning efficiency, an asymmetrical lateral PN junction is employed to enable electrical tuning of the grating based on the plasma dispersion effect. As shown in Fig. 18(b), the PN junction is slightly shifted to the left from the center of the waveguide by 50 nm, to increase the mode overlap with the p-type doping region, since the plasma dispersion effect is more sensitive to the change of the free-hole concentration. Additional p^{++} and n^{++} implantations, 1 μm away from the rib to minimize absorption losses, are posed for ohmic contact formation. Fig. 18(c) provides the top view of the grating structure on the rib and the Fabry-Perot (FP) cavity. The periodic sidewall corrugations with a depth of 75 nm are introduced to the rib. To enable the device to work in the C band, the grating period Λ is designed to be 310 nm with a duty cycle of 50%. The total length of the grating is 1240 μm, and the FP cavity, with a length L of 24.025 μm, is allocated at the center of the grating. Fig. 18(d) shows the schematic layout of the device. Two contact windows are opened on the silica pads, with 2-μm-thick aluminum layer deposited to make the contacts. The device is fabricated using a CMOS-compatible process with 248-nm deep ultraviolet lithography.

Spectral measurement in Fig. 19(a) shows that the notch in the reflection band has approximately 46 pm with a Q-factor of 33,500, and an extinction ratio is 16.4 dB. DC performance of the SBG-FPF in Fig. 19(b) and (c) shows that the average central wavelength shift rates for a forward and reverse bias are -1.15 nm/V and 4.2 pm/V, respectively. Since the light-confining resonating structure of the FP cavity can enhance the effect of refractive index change, the SBG-FPF can be employed as an electro-optic modulator. Fig. 19(d) shows the transmission window of the SBG-FPF when a reverse-bias voltage of 8.0 V is applied, and three circles are used to indicate the different input wavelengths. Fig. 19(e) shows the electro-optic frequency response for the three different input wavelengths. As can be seen, the maximum 3-dB modulation bandwidth is 5.6 GHz, and with the wavelength of the input light further away from the resonance wavelength, the measured 3-dB modulation bandwidth is becoming larger.

Fast electrical tuning speed and large tuning range make the SBG-FPF very suitable for photonic processing of microwave signals such as frequency-tunable microwave filtering, fractional-order tunable temporal differentiation, Hilbert transformation and microwave phase shifting. For example, by using the SBG-FPF as an optical notch filter to filter out one sideband of a phase modulated optical signal, a bandpass microwave filter can be implemented. In addition, by using the SBG-FPF, a fractional-order tunable temporal differentiator can be implemented.

IV. Conclusion

An overview about the recent work on silicon-based integrated microwave photonics was presented, with an emphasis on silicon-based on-chip photonic microwave waveform generation and on-chip photonic microwave signal processing. Silicon photonics provides an excellent platform for the integration of microwave photonic functionalities and systems since it leverages the mature CMOS technology with a high yield and a low cost. As the performances of high-speed and high-efficient silicon modulators [67], [68] and on-chip Germanium photodetectors [69], [70] are improving, especially hybrid solutions to heterogeneously integrate III-V materials onto silicon photonic platform to overcome the challenge in producing light sources and amplifiers [71], [72], a promising prospect to realize a full system-level integration of microwave photonic functionalities and systems on a single chip is coming.

Acknowledgments

The authors acknowledge CMC Microsystems, for providing the design tools and enabling the fabrication of the devices.

References

[1] J. Capmany and D. Novak, "Microwave photonics combines two worlds," *Nature Photon.*, vol. 1, no. 6, pp. 319–330, Apr. 2007.
[2] A. J. Seeds, "Microwave photonics," *IEEE Trans. Microw. Theory Techn.*, vol. 50, no. 3, pp. 877–887, Mar. 2002.
[3] A. J. Seeds and K. J. Williams, "Microwave photonics," *J. Lightw. Technol.*, vol. 24, no. 12, pp. 4628–4641, Dec. 2006.
[4] J. Yao, "Microwave photonics," *J. Lightw. Technol.*, vol. 27, no. 3, pp. 314–335, Feb. 1, 2009.
[5] J. Yao, "A tutorial on microwave photonics—Part I," *IEEE Photon. Soc. Newslett.*, vol. 26, no. 2, pp. 4–12, Apr. 2012.
[6] J. Yao, "A tutorial on microwave photonics—Part II," *IEEE Photon. Soc. Newslett.*, vol. 26, no. 3, pp. 5–12, Jun. 2012.
[7] J. Yao, "Photonic generation of microwave arbitrary waveforms," *Opt. Commun.*, vol. 284, no. 15, pp. 3723–3736, Jul. 2011.
[8] R. A. Minasian, E. H. W. Chan, and X. Yi, "Microwave photonic signal processing," *Opt. Exp.*, vol. 21, no. 19, pp. 22918–22936, Sep. 2013.
[9] J. Capmany, J. Mora, I. Gasulla, J. Sancho, J. Lloret, and S. Sales, "Microwave photonic signal processing," *J. Lightw. Technol.*, vol. 31, no. 4, pp. 571–586, Feb. 15, 2013.
[10] R. C. Daniels and R. W. Heath, "60 GHz wireless communications: Emerging requirements and design recommendations," *IEEE Veh. Technol. Mag.*, vol. 2, no. 3, pp. 41–50, Sep. 2007.
[11] R. Skaug and J. F. Hjelmstad, *Spread Spectrum in Communication*. London, U.K.: Peregrinus, 1985.
[12] A. W. Rihaczek, *Principles of High-Resolution Radar*. Norwood, MA, USA: Artech House, 1996.
[13] H. D. Griffiths and W. J. Bradford, "Digital generation of high time-bandwidth product linear FM waveforms for radar altimeters," *IEE Proc. F Radar Signal Process.*, vol. 139, no. 2, pp. 160–169, Apr. 1992.
[14] H. Kwon and B. Kang, "Linear frequency modulation of voltage-controlled oscillator using delay-line feedback," *IEEE Microw. Wireless Compon. Lett.*, vol. 15, no. 6, pp. 431–433, Jun. 2005.
[15] Y. Zhang and S. Pan, "Generation of phase-coded microwave signals using a polarization-modulator-based photonic microwave phase shifter," *Opt. Lett.*, vol. 38, no. 5, pp. 766–768, Mar. 2013.
[16] L. X. Wang, W. Li, H. Wang, J. Y. Zheng, J. G. Liu, and N. H. Zhu, "Photonic generation of phase coded microwave pulses using cascaded polarization modulators," *IEEE Photon. Technol. Lett.*, vol. 25, no. 7, pp. 678–681, Apr. 1, 2013.

[17] W. Li and J. Yao, "Generation of linearly chirped microwave waveform with an increased time-bandwidth product based on a tunable optoelectronic oscillator and a recirculating phase modulation loop," *J. Lightw. Technol.*, vol. 32, no. 20, pp. 3573–3579, Oct. 15, 2014.

[18] P. Ghelfi, F. Scotti, F. Laghezza, and A. Bogoni, "Photonic generation of phase-modulated RF signals for pulse compression techniques in coherent radars," *J. Lightw. Technol.*, vol. 30, no. 11, pp. 1638–1644, Jun. 1, 2012.

[19] J.-W. Shi, F.-M. Kuo, N.-W. Chen, S. Y. Set, C.-B. Huang, and J. E. Bowers, "Photonic generation and wireless transmission of linearly/nonlinearly continuously tunable chirped millimeter-wave waveforms with high time-bandwidth product at W-band," *IEEE Photon. J.*, vol. 4, no. 1, pp. 215–223, Feb. 2012.

[20] A. Zeitouny, S. Stepanov, O. Levinson, and M. Horowitz, "Optical generation of linearly chirped microwave pulses using fiber Bragg gratings," *IEEE Photon. Technol. Lett.*, vol. 17, no. 3, pp. 660–662, Mar. 2005.

[21] H. Gao, C. Lei, M. Chen, F. Xing, H. Chen, and S. Xie, "A simple photonic generation of linearly chirped microwave pulse with large time-bandwidth product and high compression ratio," *Opt. Exp.*, vol. 21, no. 20, pp. 23107–23115, Oct. 2013.

[22] J. D. McKinney, D. E. Leaird, and A. M. Weiner, "Millimeter-wave arbitrary waveform generation with a direct space-to-time pulse shaper," *Opt. Lett.*, vol. 27, no. 15, pp. 1345–1347, Aug. 2002.

[23] I. S. Lin, J. D. McKinney, and A. M. Weiner, "Photonic synthesis of broadband microwave arbitrary waveforms applicable to ultra-wideband communication," *IEEE Microw. Wireless Compon. Lett.*, vol. 15, no. 4, pp. 226–228, Apr. 2005.

[24] J. Chou, Y. Han, and B. Jalali, "Adaptive RF-photonic arbitrary waveform generator," *IEEE Photon. Technol. Lett.*, vol. 15, no. 4, pp. 581–583, Apr. 2003.

[25] C. Wang and J. Yao, "Chirped microwave pulse generation based on optical spectral shaping and wavelength-to-time mapping using a Sagnac loop mirror incorporating a chirped fiber Bragg grating," *J. Lightw. Technol.*, vol. 27, no. 16, pp. 3336–3341, Aug. 15, 2009.

[26] J. Zhang, O. L. Coutinho, and J. Yao, "Photonic generation of a linearly chirped microwave waveform with long temporal duration using a dispersive loop," in *Proc. IEEE MIT-S IMS*, Phoenix, AZ, USA, May 2015, pp. 1–3.

[27] M. Li and J. Yao, "Photonic generation of continuously tunable chirped microwave waveforms based on a temporal interferometer incorporating an optically pumped linearly chirped fiber Bragg grating," *IEEE Trans. Microw. Theory Techn.*, vol. 59, no. 12, pp. 3531–3537, Dec. 2011.

[28] X. Xue, X. Zheng, H. Zhang, and B. Zhou, "Widely tunable single-bandpass microwave photonic filter employing a non-sliced broadband optical source," *Opt. Exp.*, vol. 19, no. 19, pp. 18423–18429, Sep. 2011.

[29] J. Azaña, "Ultrafast analog all-optical signal processors based on fiber-grating devices," *IEEE Photon. J.*, vol. 2, no. 3, pp. 359–386, Jun. 2010.

[30] H. Shahoei, P. Dumais, and J. Yao, "Continuously tunable photonic fractional Hilbert transformer using a high-contrast Germanium-doped silica-on-silicon microring resonator," *Opt. Lett.*, vol. 39, no. 9, pp. 2778–2781, May 2014.

[31] A. Altaqui, E. H. W. Chan, and R. A. Minasian, "Microwave photonic mixer with high spurious-free dynamic range," *Appl. Opt.*, vol. 53, no. 17, pp. 3687–3695, Jun. 2014.

[32] W. Zhang and J. Yao, "Ultrawideband RF photonic phase shifter using two cascaded polarization modulators," *IEEE Photon. Technol. Lett.*, vol. 26, no. 9, pp. 911–914, May 1, 2014.

[33] J. Yao, F. Zeng, and Q. Wang, "Photonic generation of ultrawideband signals," *J. Lightw. Technol.*, vol. 25, no. 11, pp. 3219–3235, Dec. 2007.

[34] F. Li, Y. Park, and J. Azaña, "Complete temporal pulse characterization based on phase reconstruction using optical ultrafast differentiation (PROUD)," *Opt. Lett.*, vol. 32, no. 22, pp. 3364–3366, Nov. 2007.

[35] D. Marpaung, C. Roeloffzen, R. Heideman, A. Leinse, S. Sales, and J. Capmany, "Integrated microwave photonics," *Lasers Photon. Rev.*, vol. 7, no. 4, pp. 506–538, Jul. 2013.

[36] M. S. Rasras *et al.*, "Demonstration of a tunable microwave-photonic notch filter using low-loss silicon ring resonators," *J. Lightw. Technol.*, vol. 27, no. 12, pp. 2105–2110, Jun. 15, 2009.

[37] J. Cardenas *et al.*, "Wide-bandwidth continuously tunable optical delay line using silicon microring resonators," *Opt. Exp.*, vol. 18, no. 25, pp. 26525–26534, Dec. 2010.

[38] M. H. Khan *et al.*, "Ultrabroad-bandwidth arbitrary radiofrequency waveform generation with a silicon photonic chip-based spectral shaper," *Nature Photon.*, vol. 4, no. 2, pp. 117–122, Feb. 2010.

[39] M. Ferrera *et al.*, "On-chip CMOS-compatible all-optical integrator," *Nature Commun.*, vol. 1, no. 29, pp. 1–5, May 2010.

[40] E. J. Norberg, R. S. Guzzon, J. S. Parker, L. A. Johansson, and L. A. Coldren, "Programmable photonic microwave filters monolithically integrated in InP–InGaAsP," *J. Lightw. Technol.*, vol. 29, no. 11, pp. 1611–1619, Jun. 1, 2011.

[41] J. C. Hulme *et al.*, "Fully integrated hybrid silicon two dimensional beam scanner," *Opt. Exp.*, vol. 23, no. 5, pp. 5861–5874, Mar. 2015.

[42] R. S. Guzzon, E. J. Norberg, and L. A. Coldren, "Spurious-free dynamic range in photonic integrated circuit filters with semiconductor optical amplifiers," *IEEE J. Quantum Electron.*, vol. 48, no. 2, pp. 269–278, Feb. 2012.

[43] W. Bogaerts *et al.*, "Silicon microring resonators," *Laser Photon. Rev.*, vol. 6, no. 1, pp. 47–73, Jan. 2012.

[44] W. Zhang, J. Zhang, and J. Yao, "Largely chirped microwave waveform generation using a silicon-based on-chip optical spectral shaper," in *Proc. MWP*, Sapporo, Japan, Oct. 2014, pp. 51–53.

[45] H. Yun, W. Shi, Y. Wang, L. Chrostowski, and N. A. F. Jaeger, "2×2 Adiabatic 3-dB coupler on silicon-on-insulator rib waveguides," *Proc. SPIE*, vol. 8915, paper 89150V, May 2013.

[46] W. Bogaerts and S. K. Selvaraja, "Compact single-mode silicon hybrid rib/strip waveguide with adiabatic bends," *IEEE Photon. J.*, vol. 3, no. 3, pp. 422–432, Jun. 2011.

[47] W. Zhang and J. Yao, "Photonic generation of linearly chirped microwave waveform with a large time-bandwidth product using a silicon-based on-chip spectral shaper," in *Proc. MWP*, Paphos, Cyprus, Oct. 2015.

[48] W. Zhang and J. Yao, "Photonic generation of linearly chirped microwave waveforms using a silicon-based on-chip spectral shaper incorporating two linearly chirped waveguide Bragg gratings," *J. Lightw. Technol.*, vol. 33, no. 24, pp. 5047–5054, Dec. 2015.

[49] Y. Zhang *et al.*, "A compact and low loss Y-junction for submicron silicon waveguide," *Opt. Exp.*, vol. 21, no. 1, pp. 1310–1316, Jan. 2013.

[50] I. Giuntoni *et al.*, "Continuously tunable delay line based on SOI tapered Bragg gratings," *Opt. Exp.*, vol. 20, no. 10, pp. 11241–11246, May 2012.

[51] M. Spasojevic and L. R. Chen, "Discretely tunable optical delay lines using serial and step-chirped sidewall Bragg gratings in SOI," *Electron. Lett.*, vol. 49, no. 9, pp. 608–610, Apr. 2013.

[52] D. K. Hunter, M. C. Chia, and I. Andonovic, "Buffering in optical packet switches," *J. Lightw. Technol.*, vol. 16, no. 12, pp. 2081–2094, Dec. 1998.

[53] S. Blais and J. Yao, "Photonic true-time delay beamforming based on superstructured fiber Bragg gratings with linearly increasing equivalent chirps," *J. Lightw. Technol.*, vol. 27, no. 9, pp. 1147–1154, May 1, 2009.

[54] A. Melloni *et al.*, "Tunable delay lines in silicon photonics: Coupled resonators and photonic crystals, a comparison," *IEEE Photon. J.*, vol. 2, no. 2, pp. 181–194, Apr. 2010.

[55] S. Mallat, *A Wavelet Tour of Signal Processing*. San Diego, CA, USA: Academic, 1999.

[56] X. Wang, W. Shi, R. Vafaei, N. A. F. Jaeger, and L. Chrostowski, "Uniform and sampled Bragg gratings in SOI strip waveguides with sidewall corrugations," *IEEE Photon. Technol. Lett.*, vol. 23, no. 5, pp. 290–292, Mar. 1, 2011.

[57] R. A. Soref and B. R. Bennett, "Electrooptical effects in silicon," *IEEE J. Quantum Electron.*, vol. 23, no. 1, pp. 123–129, Jan. 1987.

[58] C. Cuadrado-Laborde and M. V. Andrés, "In-fiber all-optical fractional differentiator," *Opt. Lett.*, vol. 34, no. 6, pp. 833–835, Mar. 2009.

[59] C. Cuadrado-Laborde, "All-optical ultrafast fractional differentiator," *Opt. Quantum Electron.*, vol. 40, no. 13, pp. 983–990, Oct. 2009.

[60] N. K. Berger, B. Levit, B. Fischer, M. Kulishov, D. V. Plant, and J. Azaña, "Temporal differentiation of optical signals using a phase-shifted fiber Bragg grating," *Opt. Exp.*, vol. 15, no. 2, pp. 371–381, Jan. 2007.

[61] H. Shahoei, J. Albert, and J. Yao, "Tunable fractional order temporal differentiator by optically pumping a tilted fiber Bragg grating," *IEEE Photon. Technol. Lett.*, vol. 24, no. 9, pp. 370–372, May 1, 2012.

[62] W. Zhang, W. Li, and J. Yao, "Optical differentiator based on an integrated sidewall phase-shifted Bragg grating," *IEEE Photon. Technol. Lett.*, vol. 26, no. 23, pp. 2383–2386, Dec. 1, 2014.

[63] W. Zhang, W. Liu, W. Li, H. Shahoei, and J. Yao, "Independently tunable multichannel fractional-order temporal differentiator based on a silicon-photonic symmetric Mach–Zehnder interferometer incorporating cascaded microring resonators," *J. Lightw. Technol.*, vol. 33, no. 2, pp. 361–367, Jan. 15, 2015.

[64] G. P. Agrawal, *Fiber-Optic Communication Systems*, 3rd ed. New York, NY, USA: Wiley, 2002.

[65] L.-W. Luo, G. S. Wiederhecker, K. Preston, and M. Lipson, "Power insensitive silicon microring resonators," *Opt. Lett.*, vol. 37, no. 4, pp. 590–592, Feb. 2012.

[66] W. Zhang, N. Ehteshami, W. Liu, and J. Yao, "Silicon-based on-chip electrically tunable sidewall Bragg grating Fabry–Perot filter," *Opt. Lett.*, vol. 40, no. 13, pp. 3153–3156, Jun. 2015.
[67] D. J. Thomson *et al.*, "High contrast 40 Gbit/s optical modulation in silicon," *Opt. Exp.*, vol. 19, no. 12, pp. 11507–11516, Jun. 2011.
[68] F. Y. Gardes *et al.*, "High-speed modulation of a compact silicon ring resonator based on a reverse-biased pn diode," *Opt. Exp.*, vol. 17, no. 24, pp. 21986–21991, Nov. 2009.
[69] M. W. Geis, S. J. Spector, M. E. Grein, J. U. Yoon, D. M. Lennon, and T. M. Lyszczarz, "Silicon waveguide infrared photodiodes with >35 GHz bandwidth and phototransistors with 50 AW^{-1} response," *Opt. Exp.*, vol. 17, no. 7, pp. 5193–5204, Mar. 2009.
[70] D. Ahn *et al.*, "High performance, waveguide integrated Ge photodetectors," *Opt. Exp.*, vol. 15, no. 7, pp. 3916–3921, Apr. 2007.
[71] A. W. Fang, H. Park, O. Cohen, R. Jones, M. J. Paniccia, and J. E. Bowers, "Electrically pumped hybrid AlGaInAs-silicon evanescent laser," *Opt. Exp.*, vol. 14, no. 20, pp. 9203–9210, Sep. 2006.
[72] G. Roelkens, D. Van Thourhout, R. Baets, R. Nötzel, and M. Smit, "Laser emission and photodetection in an InP/InGaAsP layer integrated on and coupled to a silicon-on-insulator waveguide circuit," *Opt. Exp.*, vol. 14, no. 18, pp. 8154–8159, Sep. 2006.

Weifeng Zhang (S'12) received the B.Eng. degree in electronic science and technology from Xi'an Jiaotong University, Xi'an, China, in 2008, and the M.A.Sc. degree in electrical engineering from the Politecnico di Torino, Turin, Italy, in 2011. He is currently pursuing the Ph.D. degree with the Microwave Photonics Research Laboratory, School of Electrical Engineering and Computer Science, University of Ottawa, Ottawa, ON, Canada.

His current research interests include silicon photonics and its applications in microwave photonics.

Jianping Yao (M'99–SM'01–F'12) received the Ph.D. degree in electrical engineering from the Université de Toulon, Toulon, France, in 1997. He joined the School of Electrical and Electronic Engineering, Nanyang Technological University, Singapore, as an Assistant Professor in 1998. In 2001, he joined the School of Electrical Engineering and Computer Science, University of Ottawa, as an Assistant Professor, where he became an Associate Professor in 2003, and a Full Professor in 2006. He was appointed as the University Research Chair in Microwave Photonics in 2007. From 2007 to 2010, he was the Director of the Ottawa-Carleton Institute for Electrical and Computer Engineering. He was re-appointed as the Director of the Ottawa-Carleton Institute for Electrical and Computer Engineering in 2013. He is a Professor and University Research Chair with the School of Electrical Engineering and Computer Science, University of Ottawa, Ottawa, ON, Canada.

He has authored over 500 papers, including more than 290 papers in peer-reviewed journals and 210 papers in conference proceedings. He was a Guest Editor of the *Focus Issue on Microwave Photonics in Optics Express* in 2013 and a Feature Issue on Microwave Photonics in Photonics Research in 2014. He is currently a Topical Editor for Optics Letters, and serves on the Editorial Board of the IEEE TRANSACTIONS ON MICROWAVE THEORY AND TECHNIQUES and *China Science Bulletin*, and the Advisory Editorial Board of *Optics Communications*. He is the Chair of numerous international conferences, symposia, and workshops, including the Vice-TPC Chair of the 2007 IEEE Microwave Photonics Conference, TPC Co-Chair of the 2009 and 2010 Asia-Pacific Microwave Photonics Conferences, the TPC Chair of the High-Speed and Broadband Wireless Technologies Subcommittee of the 2009-2012 IEEE Radio Wireless Symposia, the Microwave Photonics Subcommittee of the 2009 IEEE Photonics Society Annual Meeting, and the 2010 IEEE Microwave Photonics Conference, and the General Co-Chair of the 2011 IEEE Microwave Photonics Conference. He received the 2005 International Creative Research Award at the University of Ottawa. He was a recipient of the 2007 George S. Glinski Award for Excellence in Research. He was selected to receive an Inaugural OSA Outstanding Reviewer Award in 2012. He is an IEEE MTT-S Distinguished Microwave Lecturer from 2013 to 2015.

Dr. Yao is a Registered Professional Engineer of Ontario. He is a fellow of the Optical Society of America and the Canadian Academy of Engineering.